Nondestructive Evaluation of Microwave-Penetrable Pipes by Synthetic Aperture Imaging enhanced by Full-Wave Field Propagation Model

Jaime Laviada, Baolong Wu, Mohammad Tayeb Ghasr, *Senior Member, IEEE*, and Reza Zoughi, *Fellow, IEEE*

***Abstract*—A qualitative approach for microwave imaging multi-layered cylindrical structures (e.g., dielectric pipes) is proposed in this paper. This approach relies on a modified circular synthetic aperture imaging technique that exploits closed-form Green's function to account for the different propagation delays, internal reflections and refractions. The image can then be computed by employing a matched-filter expressed in terms of efficient Fourier Transforms. Consequently, a high-resolution and contactless approach for the inspection of this kind of structures is achieved. Moreover, the computational resources to render the images are negligible. Practical aspects of the technique such as sampling criteria, resolution and limitations of the technique are discussed. The efficacy of the method is illustrated via several examples including imaging of objects and anomalies inside different types of dielectric pipes.**

***Index Terms*—nondestructive evaluation, pipe inspection, microwave imaging, synthetic aperture radar (SAR), circular SAR, deconvolution, Green's function.**

I. Introduction

Cylindrical multi-layered structures are found to be used in a wide variety of applications, commonly associated with pipes carrying different fluids and gases, storage tanks in oil and petrochemical industries and those used in power generation and utilities, to name a few. These structures are usually made of ferrous or electrically insulating (dielectric) materials such as; plastics, rubber, fiberglass, high-density polyethylene or HDPE, etc. In-service damage is a common occurrence in these pipes (e.g., internal corrosion, wall thinning, localized damage, pitting, etc.) presenting a certain risk of failure which in some instances could be catastrophic [1], [2]. Although external damages are readily detected visually, internal defects are not. Consequently, detecting internal manufacturing or in-service damages requires a robust nondestructive detection methodology.

Depending on the nature of the problem, different approaches have been proposed. For example, eddy currents have shown to be a very valuable tool to check the integrity of ferrous pipes [3]. Quality inspection of ferromagnetic pipes can also been performed by means of guided-wave methods [4]. Moreover, if the inner volume of the pipe is accessible, then a large number of endoscopic approaches based on different kind of sensors is also available [5], [6], [7], [8].

However, to the best's authors knowledge contactless and nondestructive tools, optimized for inspecting *multilayered insulating pipes*, are not available. The ability of microwave signals to readily penetrate insulating materials makes them a great candidate for inspecting dielectric composite structures [9]. This, coupled with using wideband Synthetic Aperture Radar (SAR) imaging techniques [10], which nowadays require relatively simple instrumentation, has proven to be a versatile approach for high-resolution nondestructive inspection of a host of materials and structures. In addition, SAR imaging does not require significant computational resources compared to quantitative imaging techniques [11]. Although this may be at the expense of considering certain approximations in practical terms SAR images produce highly useful images, particularly for nondestructive testing (NDT) applications [9].

The utility of SAR imaging was originally intended and formulated for free-space conditions [10]. Consequently, appropriate corrections must be made when dealing with inhomogeneous (i.e., multi-layered) materials. For multi-layered (i.e., inhomogeneous) structures, an approximate approach has been used where the average permittivity of the structure is incorporated in the imaging algorithm [12]. The utility of this method is rather limited, since average permittivity calculation does not properly account for the overall properties of the structure. However, a more effective approach involves the use of a piecewise approach or using Green's function by which much higher quality images with properly-identified internal anomalies can be produced [13], [14].

In the special case of *planar multilayered structures*, some specific approaches are available to account for the different propagation velocities and travel paths through the material (i.e., refraction). For example, a ray-tracing approach to estimate the phase of the incident and scattered fields was proposed in [15]. However, that approach is somewhat approximate as it does not properly account for multiple reflections within the layers. This limitation can be overcome by recasting the SAR imaging approach as the convolution of an unknown target distribution, usually referred to as the reflectivity function, with the corresponding Green's function for planar multilayered media [16]. Thus, the unknown function, which depicts the target structural composition, can be computed by

This work has been partially supported by the Ministerio de Ciencia e Innovación of Spain /FEDER under project TEC2014-55290-JIN.

J. Laviada is with the Department of Electrical Engineering, University of Oviedo, Gijón, 33203, Spain.

B. Wu is with the Department of Electrical Engineering, University of Electronic Science and Technology of China and was a visiting scholar at Missouri University of Science and Technology. (e-mail: wubaolongyou@163.com).

M.T. Ghasr and R. Zoughi are with the Applied Microwave Nondestructive Testing Laboratory (amntl), Missouri University of Science and Technology, Rolla, MO 65409 USA. (e-mail: [mtg7w6][Zoughi]@mst.edu).

implementing an efficient deconvolution approach [13].

Nevertheless, SAR-compatible approaches have not yet been developed for multi-layered cylindrical media. Consequently, in this paper, a SAR-based approach is developed by taking into account the different propagation mechanisms for the incident and scattered fields. In addition, limitations of the formulation are outlined and discussed. Furthermore, closed-form or numerical criteria are derived to set the sampling steps as well as an estimation of the image resolution and secondary side-lobe levels.

II. Modified Circular Synthetic Aperture Imaging

A. Multi-Layered Cylindrical Synthetic Aperture Imaging

In this paper, the imaging of embedded objects inside (infinitely) long cylinders with circular cross-sections, made of one or several different layers is considered. In practice, this type of problem is encountered in cylindrical structures such as a pipes or tanks when manufactured or in-service produced anomalies or defects, such as: air voids, eroded or damaged interior walls, are present. In order to perform the data collection for producing an image, a cylindrical scanning is therefore desired. In addition, acquisition of monostatic reflection coefficient by means of a probe (i.e., an open-ended rectangular waveguide) at regular spacing along ϕ and z (in the cylindrical coordinate system) is preferred. Monostatic approach is less complex than a multi-static approach [17] as it requires simpler measurement setup.

Fig. 1 shows a schematic of imaging data acquisition configuration in the cylindrical coordinate system. The cylindrical structure in Fig. 1 is composed of four-layers, an external layer (i.e., background medium - typically air), the most inner layer (e.g., a fluid flowing along the pipe) and two inner layers intrinsic to the construction of a typical cylindrical structure of this type.

Fig. 1. Schematic of a four-layer cylindrical structure and data acquisition configuration depicting equally-spaced imaging data acquisition points.

In the case of multi-layered structures, conventional free-space SAR approach cannot be employed, since it does not consider the corresponding propagation mechanisms such as different propagation delays (paths), refractions and reflections at various boundaries [10]. Consequently, to account for these effects, implementation of Green's function for cylindrical multi-layered structures is considered here, in a similar fashion to that implemented in [13]. To this end, let's consider a point target located at an arbitrary radial distance of $\vec{r}$, as shown in Fig. 1. If an infinitesimal dipole source emitting a monochromatic wave at angular frequency ω is located at $\vec{r}'$ (corresponding to the measurement points in Fig. 1), then the field at the point target is given by the Green's function of the corresponding medium denoted as $G_f\left(\vec{r},\vec{r}',\omega\right)$. Subscript f indicates the Green's function model for the forward propagating wave. This point target scatters the impinging wave with a complex amplitude directly proportional to the point target reflectivity, $\Gamma\left(\vec{r}\right)$, which is subsequently received at the observation point, located at $\vec{r}'$ in the considered monostatic configuration, weighted by the backward Green's function denoted by $G_b\left(\vec{r}',\vec{r},\omega\right)$. Thus, the received field can be expressed by superposition as [13]:

$$s\left(\vec{r}',\omega\right)=\int\Gamma\left(\vec{r}\right)G_{rt}\left(\vec{r},\vec{r}',\omega\right)dV, \tag{1}$$

wherein $G_{rt}=G_fG_b$ is defined as the two-way Green's function [13]. Equation (1), which is the starting point of the presented approach, and is derived in a similar fashion to the conventional SAR imaging method. This results in neglecting some of the wave interactions, including no coupling and reflections between the different areas of the structure under test, and shadowing effect due an embedded object blocking the impinging wave. Finally, the formulation assumes that the source is an ideal infinitesimal dipole. Consequently, there are some expected discrepancies between the assumed incident field in the formulation and that which may be used in practice (e.g., using an open-ended rectangular waveguide probe). However, the influence of this last issue is significantly mitigated when the cylindrical structure under test is in the far-field of the probe, since in this situation both the theoretical and actual incident fields will be (locally) very nearly a spherical wave. Considering the cylindrical symmetry of the problem, the two-way Green's function can be expressed as $G_{rt}\left(\rho',\phi',z',\rho,\phi,z,\omega\right)=G_{rt}\left(\rho',\rho,\Delta\phi,\Delta z,\omega\right)$, where $\Delta\phi=\phi-\phi'$ and $\Delta z=z-z'$. Consequently, (1) can be re-casted in cylindrical coordinate system, (ρ,ϕ,z), as:

$$s\left(\vec{r}',\omega\right)=\int\rho\Gamma\left(\rho,\phi,z\right)G_{rt}\left(\rho',\rho,\Delta\phi,\Delta z,\omega\right)d\phi dzd\rho. \tag{2}$$

To begin the process, let us assume that a target is initially located at a given radius ρ_0, which results in (2) being expressed as the following convolution:

$$s_0\left(\rho',\phi',z',\omega\right)=\rho_0\Gamma\left(\rho_0,\phi',z'\right)*G_{rt}\left(\rho',\rho_0,\phi',z',\omega\right), \tag{3}$$

where, s_0 is the monostatic acquired image data (i.e., field) due to a target (or targets) at radius$\rho=\rho_0$, and the convolution operates along ϕ and z. Consequently, the reflectivity can be estimated by solving the inverse problem modeled by (3). In this paper, a *matched-filter* approach is employed, similar to the one proposed in [18] for the time-domain source

localization. Other approaches such as Wiener deconvolution [13] are expected to render similar results. Subsequently,

$$\hat{\Gamma}(\rho,\phi,z,\omega) \approx \mathcal{F}^{-1}\left\{\tilde{s}(\rho',k_\phi,k_z,\omega)\,\tilde{G}^{*}_{rt}(\rho',\rho,k_\phi,k_z,\omega)\right\}, \quad (4)$$

where the operator $\mathcal{F}$ denotes Fourier transform along ϕ and z, $\tilde{G}_{rt}(\rho',\rho,k_\phi,k_z,\omega) = \mathcal{F}\{G_{rt}(\rho',\rho,\phi,z,\omega)\}$, $\tilde{s}(\rho',k_\phi,k_z,\omega) = \mathcal{F}\{s(\rho',\phi,z,\omega)\}$, superscript * denotes complex conjugate and $\hat{\Gamma}$ denotes the estimated reflectivity function. Although this function depends on the acquisition radius ρ', this dependency has been left out in order to simplify the notation, in addition to the fact that this acquisition radius is usually fixed in a given measurement configuration. Inserting (3) into (4), leads to the following relationship between the estimated and real reflectivity functions:

$$\hat{\Gamma}(\rho,\phi,z,\omega) = \Gamma(\rho_0,\phi,z) * \mathrm{PSF}(\rho,\rho_0,\phi,z,\omega), \quad (5)$$

$$\mathrm{PSF}(\rho,\rho_0,\phi,z,\omega) = \mathcal{F}^{-1}\left\{\tilde{G}_{rt}(\rho',\rho_0,k_\phi,k_z,\omega)\,\tilde{G}^{*}_{rt}(\rho',\rho,k_\phi,k_z,\omega)\right\} \quad (6)$$

is the point-spread function (PSF) for the circle ρ_0. The dependency of this function to ρ', has also been left off of the notation, for the same reasons mentioned previously.

The use of a matched-filter results in the point-spread function being maximum at $z = 0$, $\phi = 0$ and $\rho = \rho_0$. Therefore, the estimated reflectivity function is expected to be, to some degree, a defocused version of the real reflectivity function. This defocusing effect will be discussed later. Thus, the final image can be obtained by evaluating (4) at several observation radii, ρ, along a given volume (e.g., between the inner and outer surface of the cylinder under test).

In practice, targets will not be placed at a single point (or radius), but most probably spread along a given range of radii. However, since the problem, under the SAR approximations [17], is linearized, then a collection of targets (or a distributed target) simply becomes a linear combination of images corresponding to each singular target. Consequently, (4) can also be applied even in the case of targets distributed at different radii.

In the case of free-space cylindrical SAR imaging, the study of the corresponding wideband PSF, which is achieved by coherently combining the single-frequency PSFs, has a resolution in the xy-plane which *only* depends on the bandwidth [10]. Thus, a similar effect is also expected for inhomogeneous (i.e., multi-layered) structures by coherently adding the single-frequencies reflectivities given by (6). Finally, the reflectivity is estimated as:

$$\Gamma_\omega(\rho,\phi,z) = \int_\omega \Gamma(\rho,\phi,z,\omega)\,d\omega, \quad (7)$$

An approach to estimate the impact of wideband measurements on resolution, sidelobes, and other parameters is discussed in Section II-C.

B. Spatial sampling considerations

In performing the measurements, the criteria for spatial sampling for monostatic backscattered field $s(\vec{r}',\omega)$ is an important issue. As shown in Fig. (1), imaging data is sampled along z and around ϕ corresponding to the required cylindrical scan. It is known that spatial bandwidth for the monostatic image data acquisition of a certain target is twice the spatial bandwidth of a bistatic data acquisition configuration (i.e., fixing the Tx and moving only the Rx) [19], [20]. Consequently, according to the spatial bandwidth for a bistatic cylindrical acquisition, which are the same as for antenna measurements [21], [22], it is straightforward to show that the sampling rules for a given cylindrical target of radius a_0 are:

$$\Delta z = \frac{\lambda}{4} \qquad \Delta\phi = \frac{\lambda}{4a_0} \quad (8)$$

and the corresponding bandwidths are $W_z = 2k_0$ and $W_\phi = 2k_0a_0$. It is important to note that the sampling step along ϕ does not depend on the acquisition radius ρ', and is only dependent on the radius of the cylinder enclosing the object under test. It is also relevant to observe that these steps are rigorously derived without resorting to SAR approximations, which means they are valid not only for SAR imaging but also for quantitative inverse scattering problems [11].

In practice, these spatial bandwidths represent the upper bound limits which lead to conservative sampling steps. More precise bandwidth results, tailored for each problem under test, can be obtained from numerical analysis of the scattered field, by setting the field as:

$$s(\vec{r}',\omega) = G_{rt}(\rho',\rho_0,\phi',z',\omega) \quad (9)$$

and performing the Fourier Transform for different values of the point target values ρ_0, the numerical bandwidth can be easily obtained. This point will be illustrated in the results section for different cases.

C. Resolution considerations

It is well-known that for aperture-limited planar aperture SAR (including free-space SAR) resolution expressions are functions of positions of a point target away from the aperture [17], [23], [24], [25]. In the case of free-space cylindrical SAR, the PSF, which enables to derive the maximum theoretical resolutions, is only available in closed-form for a point target at the rotation axis [10]. Consequently, resolution for targets at any other position can only be computed through numerical simulations. Thus, to the best authors' knowledge, it is not possible to derive closed-form expressions for the PSF in the case of cylindrically multi-layered structures. However, PSF can be derived following similar steps to those for the aforementioned numerical approach to estimate the spatial bandwidth. In particular, by setting the backscattered field as in (9) and applying the imaging technique describe in Section (II-A), the PSF can be obtained for point targets at different radii, ρ_0. It is important to note that by definition this PSF is derived for a point target. Consequently, it does not consider the effects of multiple reflections, blockage/shadowing, etc. Thus, even though PSF is useful as a first-order approximation,

additional artifacts, which cannot be estimated, could appear in the final image. This fact will be also illustrated in the results sections.

III. Results

In order to implement the Green's function required in (4), we followed the formulation proposed in [26] but other formulations (e.g., [16]) are expected to yield similar results. Once the Green's function has been computed, then (4) can be used to build an image of any geometry with the same layered configuration. The required CPU time, on an Intel® Xeon E5-2650v3 at 2.3 GHz, to evaluate (4) is less than 1 second for all of the examples presented here.

The results herein are provided for three different structures (geometries), each of which comprising of three different layers. Unless otherwise stated, all the results are reported considering 51 equally-spaced frequencies in the range of 8.2 GHz to 12.4 GHz (i.e., X-band). In the first structure, referred to as geom#1, in addition to the background medium with $\varepsilon_r = 1$, a cover layer represented by a lossless dielectric (i.e., plastic) with a thickness of 2 cm and $\varepsilon_r = 2$ surrounding an inner layer with a radius of 7 cm and $\varepsilon_r = 4 - j0.01$ (i.e., oil) are considered. When considering this structure, an acquisition radius of $\rho' = 15$ cm is considered. The second structure, referred to as geom#2, consists of a high-density polyethylene (HDPE) pipe. The HDPE pipe has a thickness of 2 cm, inner radius of 7.3 cm and is assumed lossless with a relative dielectric constant $\varepsilon_r = 2.4$ [27]. This pipe was filled with sand with a relative dielectric constant having been measured at X-band (8.2-12.4 GHz) to be $\varepsilon_r = 2.6 - j0.3$ (average over the band). The acquisition radius for this geometry is set to $\rho' = 25$ cm. The last structure, referred to as geom#3, is an polyvinyl chloride (PVC) pipe having an inner radius of 7.63 cm and a wall thickness of 7.7 mm, with a relative dielectric constant of $2.7 - j0.018$ [27]. The pipe is filled with tap water, which is known to have high permittivity and loss factor that are dependent on temperature and any present soluble (i.e., salts) [28]. For the considered example, the impact of several possible dielectric constant values was considered without observing a significant influence in the Green's function. Consequently, an average value of $\varepsilon_r = 60 - j25$ was used. In this case, the acquisition radius is $\rho' = 16.1$ cm. In addition, only linearly polarized antennas with electric field vectors along z are considered. Consequently, only the z-component of the dyadic Green's function need to be considered.

A. Spatial bandwidth calculation results

The spatial spectra for the described geometries are illustrated in Fig. 2. In all cases, the results are reported for the maximum available frequency in the considered range (i.e., 12.4 GHz) as it requires the smallest spatial sampling distance. Results reported in Fig. 2 are illustrated only for the sampling along the angular coordinate ϕ since linear sampling criterion along z is well-known from conventional planar aperture SAR [29]. Otherwise, a similar analysis could be repeated for that coordinate as well. As inferred from Fig. 2, the maximum spatial bandwidth does not exceed the limit given by $W_\phi = 2k_0a$, and in some cases it is significantly smaller (e.g., geom#2) enabling the possibility of increasing the spatial sampling step size depending on the geometry, and possibly the maximum radius of the cylinder enclosing the embedded object.

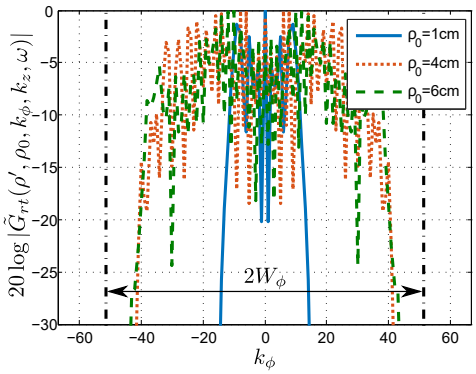

(a) geom#1

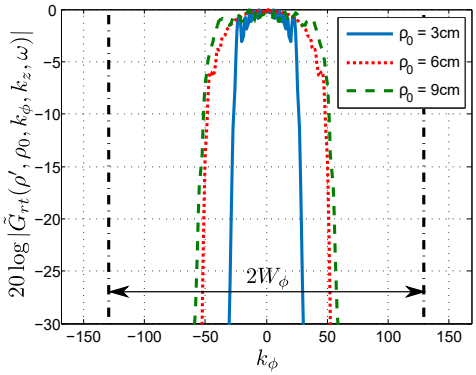

(b) geom#2

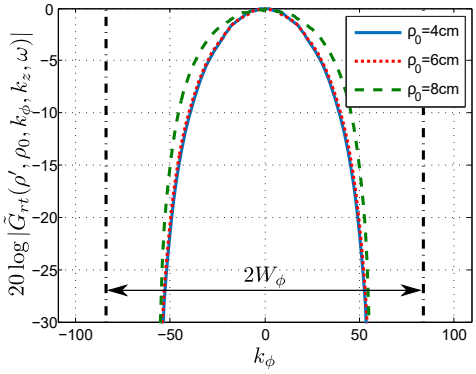

(c) geom#3

Fig. 2. Normalized spatial spectrum of the round trip Green's function along k_ϕ for different geometries.

B. Results of PSF Calculation

In order to estimate the potential quality of an image, its PSF can be numerically computed. In particular, we focus on geom#1 but a similar procedure can be followed for any other geometry. In addition, two point targets are considered in this example to illustrate the results for two different radii. These point targets are placed at $\rho_0 = 3$ cm and $\rho_0 = 4$ cm

with an angular spacing of 135º, respectively. Both targets are at the same height along the z-axis. In order to validate the correctness of the imaging technique and its results, a similar analysis is also performed by performing a full-wave simulation. In particular, geom#1 truncated at a finite height of 10 cm is simulated using the full-wave simulation software Feko [30]. The target is illuminated using an infinitesimal dipole source. The targets are modeled by perfectly electric conductor spheres of radius 1 mm (i.e., point targets). Due to the high computational resources required by the analysis of such a large structure, this analysis is limited to a circular SAR rather than a cylindrical SAR, i.e., sweeping along the z-axis is not considered. Therefore, the analysis for resolution along this axis is not considered here. Fig. 3 shows the results for the slice containing the two point targets illustrating that the targets are correctly imaged. In the case of PSF computed from Green's functions, the secondary side lobe starts at -10 dB whereas these lobes start at -7 dB for the image computed from the full-wave simulation of the finite cylinder. Due to the small size of the simulated targets, occlusions and double reflections are expected to be weak and, therefore, differences are attributed to the truncated height of the cylinder.

For the sake of completeness, the image computed from the ideal roundtrip Green's function, in (9), but using conventional circular SAR [10] with the *average* wavenumber (weighted by the radius of each layer) is shown in Fig. 4. It is clear that the resolution obtained by this method is significantly worse than the proposed method, as was previously shown for planar multi-layer geometries [13].

C. Imaging results

In order to demonstrate the practical imaging capabilities of this method, multi-layered cylinders corresponding to geom#2 and geom#3 were considered. For geom#2, two screws with a diameter of 0.5 cm and length 6 cm were inserted at different heights inside a HDPE pipe filled with sand. The measurement setup, consisting of the pipe, the probe and the turntable for the cylindrical scan, is shown in Fig. 5. An open-ended rectangular waveguide probe was used to collect calibrated reflection coefficient data at X-band (8.2-12.4 GHz) referenced to the waveguide aperture. In this case, the z-axis was sampled with 21 samples with a spacing of $\Delta z = 5$ mm whereas 121 samples were considered along ϕ.

The resulting images, computed for volume inside the pipe (i.e., $\rho_0 < 7.3$mm), are shown in Figs. 6. The modified cylindrical SAR clearly identifies the two targets at their correct positions.

Finally, geom#3 corresponding to the PVC pipe filled by water was considered. The pipe was locally damaged from the inside (simulating erosion), as shown in Fig. 7. In this case, the z-axis step was also set to $\Delta z = 5$ mm and 17 samples were considered. The same sampling as in the previous example is considered for along ϕ.

Fig. 8 depicts the reflectivity function at an inner cylinder with radius $\rho = 8$ cm, i.e., four millimeters from the inner surface. The method illustrates again that the flaw can be correctly imaged providing the potential of the method for nondestructive evaluation.

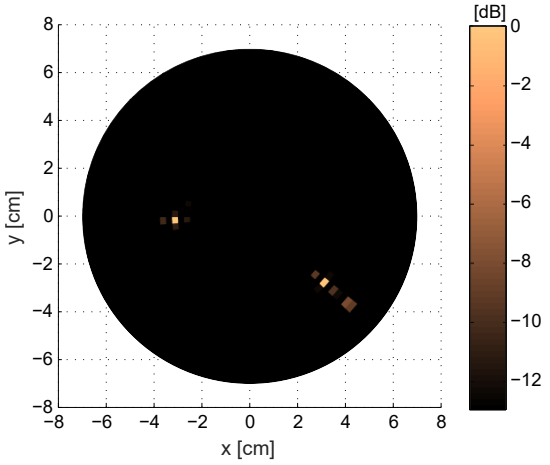

(a)

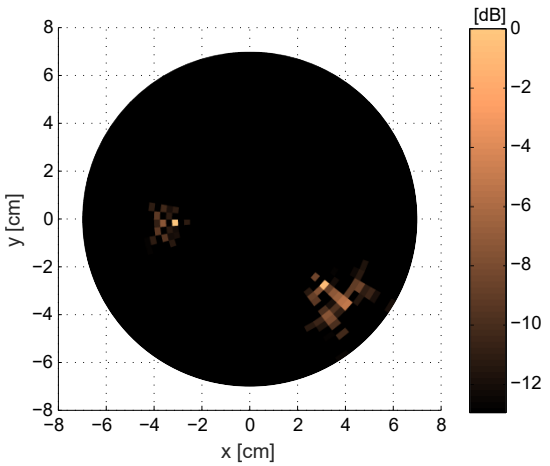

(b)

Fig. 3. Normalized estimated reflectivity $\hat{\Gamma}$ in the plane $z = 0$ using the proposed method for geom#1 with two point targets at $\rho_0 = 3$ cm and $\rho_0 = 4$ cm with an angular spacing between them of 135º. Image computed from (a) ideal roundtrip Green's function and (b) full-wave simulation of a finite cylinder.

IV. Conclusions

In this paper, we present a pipe inspection technique derived from a cylindrical SAR formulation, which takes into account cylindrically multi-layered structures. The data processing relies on approximations similar to those employed in conventional SAR for free-space but it allows for correct modeling of the propagation of the incident and scattered electromagnetic fields by employing the corresponding Green's function of the structure. Upper bounds, based on well-known results for the spatial spectrum, can be derived to estimate the sampling steps, which can be further refined by considering numerical results.

In contrast to planar aperture free-space SAR, it is not possible to derive general rules to predict resolution and sidelobe levels of the image. However, an estimation of both parameters can be easily found numerically by computing the PSF by taking advantage of the Green's function knowledge. It is interesting to observe that the sidelobe level of the image, which imposes a limit for the image dynamic range, is in general, higher than in planar-aperture free-space SAR (10 dB vs 13 dB). Despite this limitation, the imaging approach is

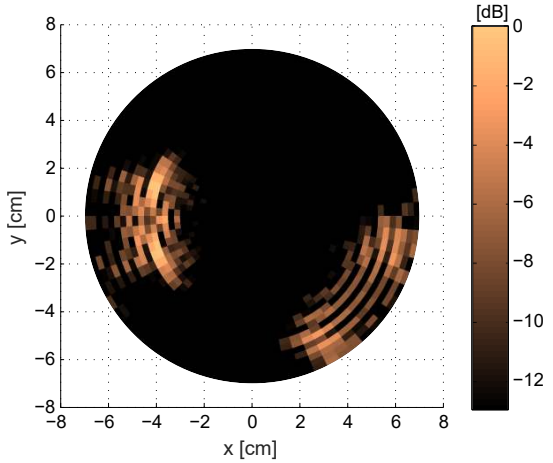

Fig. 4. Normalized estimated reflectivity $\hat{\Gamma}$ in the plane $z = 0$ for geom#1 with two point targets at $\rho_0 = 3\,\text{cm}$ and $\rho_0 = 4\,\text{cm}$ with an angular spacing between them of 135º. Image computed from ideal roundtrip Green's function and with processing corresponding to conventional circular SAR using the average wavenumber.

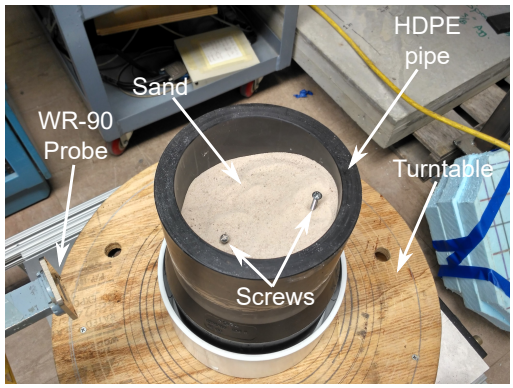

Fig. 5. HDPE pipe with two screws before being completely filled by sand.

expected to be useful in a large variety of situations such as the detection of targets inside of pipes or the detection of flaws, as presented in the measured results, facilitating its utility in nondestructive evaluation applications with electrically large stand-off distances.

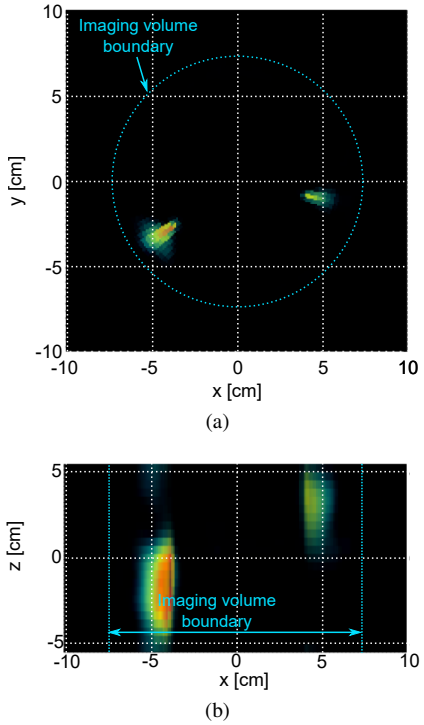

Fig. 6. Three-dimensional image of two screws inside a HDPE pipe full of sand: (a) top view, and (b) side view.

Fig. 7. PVC pipe with internal damage.

REFERENCES

[1] H. Kwun, S. Y. Kim, M. S. Choi, and S. M. Walker, "Torsional guided wave attention in coal-tar-enamel-coated, buried piping," *NDT E Int.*, vol. 37, no. 7, pp. 663–665, Dec. 2004.

[2] H. Kwun and K. A. Bartels, "Magnetostrictive sensor technology and its applications," *Ultrasonics*, vol. 36, no. 1, pp. 171–178, Feb. 1998.

[3] J. Yin, M. Lu, and J. P. de Gyvez, "Full-signature real-time corrosion detection of underground casing pipes," *IEEE Transactions on Instrumentation and Measurement*, vol. 49, no. 1, pp. 120–128, Feb 2000.

[4] D. Zhang, Z. Zhou, J. Sun, E. Zhang, Y. Yang, and M. Zhao, "A magnetostrictive guided-wave nondestructive testing method with multifrequency excitation pulse signal," *IEEE Transactions on Instrumentation and Measurement*, vol. 63, no. 12, pp. 3058–3066, Dec 2014.

[5] T. Inari, K. Takashima, M. Watanabe, and J. Fujimoto, "Optical inspection system for the inner surface of a pipe using detection of circular images projected by a laser source," *Measurement*, vol. 13, no. 2, pp. 99 – 106, 1994.

[6] A. Basu and D. Southwell, "Omni-directional sensors for pipe inspection," in *1995 IEEE International Conference on Systems, Man and Cybernetics. Intelligent Systems for the 21st Century*, vol. 4, Oct 1995, pp. 3107–3112.

[7] W. W. Zhang and B. H. Zhuang, "Non-contact laser inspection for the inner wall surface of a pipe," *Measurement Science and Technology*, vol. 9, no. 9, p. 1380, 1998.

[8] E. Wu, Y. Ke, and B. Du, "Noncontact laser inspection based on a psd for the inner surface of minidiameter pipes," *IEEE Transactions on Instrumentation and Measurement*, vol. 58, no. 7, pp. 2169–2173, July 2009.

[9] S. Kharkovsky and R. Zoughi, "Microwave and millimeter wave nondestructive testing and evaluation - overview and recent advances," *IEEE Instrum. Meas. Mag.*, vol. 10, no. 2, pp. 26–38, April 2007.

[10] M. Soumekh, *Synthetic aperture radar signal processing with MATLAB algorithms*. John Wiley & Sons, INC., 1999.

[11] M. Pastorino, *Microwave Imaging*. John Wiley & Sons, Inc., 2010.

[12] A. T. Mobashsher and A. M. Abbosh, "On-site rapid diagnosis of intracranial hematoma using portable multi-slice microwave imaging system," *Sci. Rep*, vol. 6, no. 37620, 2016.

[13] M. Fallahpour, J. T. Case, M. T. Ghasr, and R. Zoughi, "Piecewise and Wiener filter-based SAR techniques for monostatic microwave imaging of layered structures," *IEEE Trans. Antennas Propag.*, vol. 62, no. 1, pp. 282–294, Jan 2014.

[14] M. Fallahpour and R. Zoughi, "Fast 3D qualitative method for through-wall imaging and structural health monitoring," *IEEE Geoscience and*

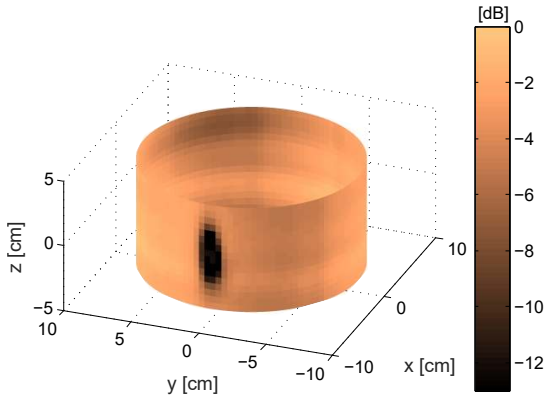

Fig. 8. Estimated normalized reflectivity function at $\rho = 8\,\text{cm}$ for the PVC pipe (geom#3) with a flaw.

Remote Sensing Letters, vol. 12, no. 12, pp. 2463–2467, Dec. 2015.

[15] S. C. Henry, L. M. Zurk, S. Schecklman, and D. D. Duncan, "Three-dimensional broadband terahertz synthetic aperture imaging," *Opt. Eng.*, vol. 51, no. 9, pp. 091 603–1–091 603–9, 2012.

[16] W. C. Chew, *Waves and Fields in Inhomogenous Media*. Wiley-IEEE Press, 1994.

[17] S. S. A. Ahmed, "Electronic microwave imaging with planar multistatic arrays," Ph.D. dissertation, Faculty of Engineering, Friedrich-Alexander-Universität Erlangen-Nürnberg, 4 2013.

[18] D. Liu, S. Vasudevan, J. Krolik, G. Bal, and L. Carin, "Electromagnetic time-reversal source localization in changing media: Experiment and analysis," *IEEE Trans. Antennas Propag.*, vol. 55, no. 2, pp. 344–354, Feb 2007.

[19] O. M. Bucci and T. Isernia, "Electromagnetic inverse scattering: Retrievable information and measurement strategies," *Radio Science*, vol. 32, no. 6, 1997.

[20] J. Laviada, Y. Álvarez-López, A. Arboleya-Arboleya, C. García-González, and F. Las-Heras, "Interferometric technique with nonredundant sampling for phaseless inverse scattering," *IEEE Trans. Antennas Propag.*, vol. 62, no. 2, pp. 739–746, Feb 2014.

[21] A. Yaghjian, "An overview of near-field antenna measurements," *IEEE Trans. Antennas Propag.*, vol. 34, no. 1, pp. 30–45, Jan 1986.

[22] F. C. Fácila and M. Sierra-Castañer, "Application of postprocessing techniques methods for noise reduction in cylindrical near field antenna measurements," in *2012 6th European Conference on Antennas and Propagation (EUCAP)*, March 2012, pp. 2555–2559.

[23] D. M. Sheen, D. L. McMakin, and T. E. Hall, "Three-dimensional millimeter-wave imaging for concealed weapon detection," *IEEE Trans. Microw. Theory Tech.*, vol. 49, no. 9, pp. 1581–1592, Sep 2001.

[24] J. M. Lopez-Sanchez and J. Fortuny-Guasch, "3-D radar imaging using range migration techniques," *IEEE Trans. Antennas Propag.*, vol. 48, no. 5, pp. 728–737, May 2000.

[25] V. Krozer, T. Loffler, J. Dall, A. Kusk, F. Eichhorn, R. K. Olsson, J. D. Buron, P. U. Jepsen, V. Zhurbenko, and T. Jensen, "Terahertz imaging systems with aperture synthesis techniques," *IEEE Trans. Microw. Theory Tech.*, vol. 58, no. 7, pp. 2027–2039, July 2010.

[26] L.-W. Li, M.-S. Leong, T.-S. Yeo, and P.-S. Kooi, "Electromagnetic dyadic Green's functions in spectral domain for multilayered cylinders," *J. Electromagn. Waves Appl.*, vol. 14, pp. 961–985, 2000.

[27] B. Riddle, J. Baker-Jarvis, and J. Krupka, "Complex permittivity measurements of common plastics over variable temperatures," *IEEE Trans. Microw. Theory Tech.*, vol. 51, no. 3, pp. 727–733, Mar. 2003.

[28] F. Ulaby, R. K. Moore, and A. K. Fung, *Microwave Remote Sensing: Active and Passive, vol. III, Volume Scattering and Emission Theory, Advanced Systems and Applications.*, Artech House Inc., Dedham, Mass., 1986.

[29] J. Case, M. Ghasr, and R. Zoughi, "Optimum 2D uniform spatial sampling for microwave SAR-based NDE imaging systems," *IEEE Transactions on Instrumentation and Measurement*, vol. 60, no. 12, pp. 3806–3815, Dec. 2011.

[30] *FEKO User Manual, Suite 7.0*. Stellenbosch, South Africa: EM Softw. Syst. S.A. (Pty) Ltd., 2014.